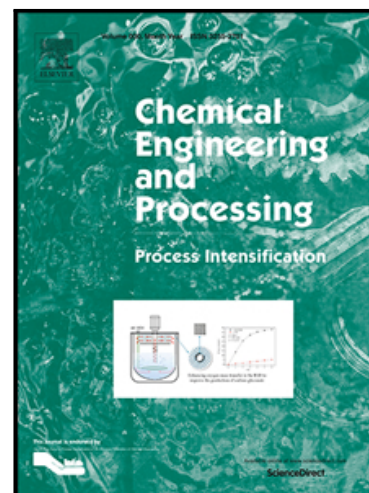# Journal Pre-proof

Numerical investigation on distribution characteristics of oxidation air in a lime slurry desulfurization system with rotary jet agitators

Longhao Xiang , Xun Sun , Xuesong Wei , Guichao Wang , Grzegorz Boczkaj , Joon Yong Yoon , Songying Chen

Please cite this article as: Longhao Xiang , Xun Sun , Xuesong Wei , Guichao Wang , Grzegorz Boczkaj , Joon Yong Yoon , Songying Chen , Numerical investigation on distribution characteristics of oxidation air in a lime slurry desulfurization system with rotary jet agitators, *Chemical Engineering and Processing - Process Intensification* (2021), doi: https://doi.org/10.1016/j.cep.2021.108372

This is a PDF file of an article that has undergone enhancements after acceptance, such as the addition of a cover page and metadata, and formatting for readability, but it is not yet the definitive version of record. This version will undergo additional copyediting, typesetting and review before it is published in its final form, but we are providing this version to give early visibility of the article. Please note that, during the production process, errors may be discovered which could affect the content, and all legal disclaimers that apply to the journal pertain.

Numerical investigation on distribution characteristics of oxidation air in a lime slurry desulfurization system with rotary jet agitators

Longhao Xiang [a,b], Xun Sun [a,b*], Xuesong Wei [a,b], Guichao Wang [a,b], Grzegorz Boczkaj [d], Joon Yong Yoon [c], and Songying Chen [a,b*]

[a] *Key Laboratory of High Efficiency and Clean Mechanical Manufacture, Ministry of Education, School of Mechanical Engineering, Shandong University, Jinan 250061, China*

[b] *National Demonstration Center for Experimental Mechanical Engineering Education, Shandong University, Jinan 250061, China*

[c] *Department of Mechanical Engineering, Hanyang University, Ansan 15588, Republic of Korea*

[d] *Department of Process Engineering and Chemical Technology, Faculty of Chemistry, Gdańsk University of Technology, Gdańsk 80-233, Poland*

[1] xlhsdu@mail.sdu.edu.cn [2] xunsun@sdu.edu.cn [3] weixuesong@sdu.edu.cn [4] wanggc@sdu.edu.cn [5] grzegorz.boczkaj@pg.edu.pl [6] joyoon@hanyang.ac.kr [7] chensy66@sdu.edu.cn

* Corresponding authors

Xun Sun and **Songying Chen**

Key Laboratory of High Efficiency and Clean Mechanical Manufacture, Ministry of Education, School of Mechanical Engineering, Shandong University

17923, Jingshi Road, Jinan, Shandong Province, 250061, People's Republic of China

Tel.: + 86-0531-88392378
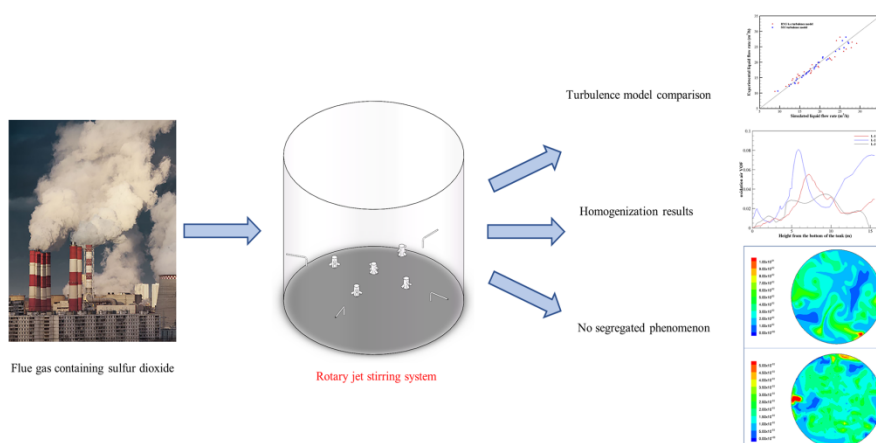
Fax: + 82-0531-88392378

Highlights

- The rotary jet agitator (RJA) is applied in agitator air lance assemblies.
- The distribution of oxidation air under different conditions was investigated.
- The optimal turbulence model of the RJA was obtained.
- The effect of rotation angular velocity and jet outlet velocity was determined.
- The homogenization of RJA is better than that of mechanical agitator.

Word Count: 4,450

Graphical abstract

Flue gas containing sulfur dioxide

Rotary jet stirring system

Turbulence model comparison

Homogenization results

No segregated phenomenon

Abstract

Rotary jet agitator is an effective device for mixing, dispersing, dissolving, and suspending dispersed phases in liquid, and is particularly advantageous to the homogenization of oxygen-enriched air within the lime slurry desulfurization system. The distribution of oxygen-enriched air in agitators is vital for the process of gypsum crystallization and the homogeneous and sufficient oxygen-enriched air can promote the formation of an economically useful by-product. The present study investigated the diffusion performance of oxygen-enriched air in a rotary jet agitator during the wet flue gas desulfurization process by utilizing computational fluid dynamics. The consistency of numerical and experimental results is validated under identical conditions. Investigation results show that the rotation velocities and the inlet velocities of rotary jet machines significantly affect the distribution and homogeneity of the oxygen-enriched air distribution. However, these effects deteriorate with increasing rotation angular and jet outlet velocities. Under the optimal condition, the oxygen-enriched air concentration, within the cross-sections, fluctuates by approximately 20%. The Rotary jet agitator appears to be a remarkable method for the

I

homogenization of oxygen-enriched air in the lime slurry tank, and in other gas-liquid stirring tanks, due to its high efficacy and good stirring effect.

Keywords: *Wet flue gas desulfurization; Lime slurry tank; Rotary jet stirring system; Computational fluid dynamics; Gas-liquid two-phase flow*

II

1. Introduction

Sulfur dioxide (SO_2) emitted from coal-fired power plants through fossil fuel combustion is one of the primary atmospheric pollutants and contributes to acid rain formation. Therefore, SO_2 is a precursor of environmental acidification, which adversely affects human health and the environment [1]. A recent study revealed that acid rain has already decimated the populations of numerous fish and plants of the lakes in the Adirondacks by 50%, and the pH values in certain lakes have reached such levels of acidity as to replace the trout and native plants with acid-tolerant rough fish species and mats of algae lakes [2]. Therefore, it is necessary to reduce the emission of SO_2 in order to mitigate the obvious air pollution problem. There are several kinds of flue gas desulfurization technologies, such as wet, dry, semi-dry, biological, and electronic processes [3-5]. Among them, wet flue gas desulfurization (WFGD) is currently the most widely used desulfurization technology, due to its high SO_2 removal efficiency, low investment, simple structure, and stable operation [6]. Gypsum crystallization is the last stage of WFGD process (Table 1), and is vital for obtaining high-quality byproducts. When the air is supplied in excess, the byproduct of WFGD is mostly gypsum, instead of hydrated calcium sulfite, which is known as forced oxidation (the corresponding oxidation reactions are demonstrated in Eqs. (3)–(9)) [4, 7]. In consequence, adequate and homogenous oxygen-enriched air in the reactor ensures that the gypsum crystallization proceeds efficiently and fully.

Jet agitator, firstly proposed by Potter [8] in 1949, is a simple and powerful stirring device used in agitator air lance assemblies, with the advantages of generating

3

tiny bubbles, small dependability on submergence depth, and high mass transfer efficiency [9]. In comparison to conventional mechanical agitators, jet agitators can produce high-speed jets and crush air bubbles, and consequently, improve the uniformity of the oxygen-enriched air [10-12]. Its effects are similar to hydrodynamic cavitation which also generates high-speed jets and disperses air within the liquid medium and is employed in numerous environmentally friendly applications [13-18]. It is found that the overall efficiency gain of the jet agitator can reach as high as 51.9% with optimal operating parameters [19]. At the early stage, experimental methods, such as tracer-decay [20], conductivity measuring [21, 22], ultrasound velocity profiling [23], and particle-image velocimetry techniques [24], are employed to explore the homogenization process in jet agitators. Even though the experiments revealed that the aeration rate and turbulence fluctuation caused by the jets can enhance the mixing process, the limitations of the measurement methods do not allow for an exact determination of distribution profiles within an agitator. Moreover, experimental researches normally culminate in the empirical equations that relate the mixing parameters to the operating conditions and geometries. Therefore, the accuracy of the empirical equations is limited by measurement accuracy.

On the contrary, physical flow features obtained by computational fluid dynamics (CFD) with suitable turbulence models are more accurate and comprehensive. Moreover, it is possible to explore the influence of the geometric structure and operating conditions on the research object via CFD [25]. The turbulence energy and dissipation rate can be captured, which can be utilized to predict the homogenization

4

pattern [26]. Therefore, it is particularly important to choose a suitable turbulence model. Researchers have compared the numerical results of jet stirring systems with different turbulence models. The RNG k-ε model is suitable for side entry and inclined side entry jet mixing tank simulations [27, 28], while for axial jet mixing tanks, the shear stress transport (SST) model, Reynolds stress model, and large eddy simulation (LES) have to be used instead of the RNG k-ε model [29, 30]. The choice of turbulence model will determine the reliability of the numerical simulation. Whereas, no literature has concerned on it for this type of agitator. The installation angle and position can significantly affect the flow field characteristics, and rotary jet machines [31, 32], which combine the features of the axial jet and inclined side entry jet, serve as jet generators in the lime slurry desulfurization system.

In this paper, the jet stirring process with an upward jet of a lime slurry tank under various working conditions was simulated by utilizing CFD. The dependability of the numerical method was validated under identical experimental conditions. The influences of the rotation and the outlet velocities on the distribution of oxygen-enriched air, which have not studied in previous literature, are analyzed, Finally, the inherent mixing laws and dynamic characteristics are explored. The corresponding findings provide strong support for the fundamental understanding and applications of rotary jet machines in the actual WFGD project.

2. Numerical method

2.1 Physical model of lime slurry stirring tank

The physical model established in this paper is based on the actual size of a lime

slurry tank of a 600 MW thermal power unit in China, as shown in Figure 1. The height and radius of the tank are 15.54 and 8.2 m, respectively. There are four non-uniform air inlet pipes arranged in the tank, which are 2.5 m away from the bottom of the stirring tank. The rotary jet machine, consisting of six evenly distributed nozzles with a diameter of 0.2 m, is driven by an internal axial flow turbine to rotate at a certain angular velocity. A pair of nozzles are arranged horizontally, while the others are slanted with an angle of 30° between the central axis and horizontal plane (Figure 1 (a)).

The flow field in the lower part of the stirring tank is predicted to be more intense than that in the upper part for the large size of the tank and the low pumping pressure, and dispersion effect of the rotary jet machine on the oxygen-enriched air is mainly concentrated in the lower part of the slurry tank, where dense grids are required in order to ensure calculational accuracy. To save computation resources, the tank is divided into upper and lower parts at one-third height from the bottom. Five rotary jet machines are installed to enhance the stirring effect. Rotary jet machines are distributed near oxygen-enriched air inlets, which is conducive to the homogenization of oxygen-enriched air (Figure 1 (b)).

2.2 Turbulence model

The jet is considered as fully turbulent flow at a jet Reynolds number, Re_j, > 1000–2000 [33]. Re_j is calculated as:

$$Re_j = \frac{\rho U d}{\mu}, \tag{10}$$

where μ is the viscosity coefficient of the fluid. In this study, Re_j is 4.36×10^6 at the

6

minimum outlet velocity. Therefore, it is necessary to choose an appropriate turbulence model to predict the high shear distortion flow field in the rotary jet stirring tank. The Reynolds-Averaged Navier-Stokes (RANS) turbulence models have shown their clear advantages for many applications, especially for wall-bounded flows [34]. Eddy-viscosity models, including k-ε and k-ω models, are a series of typical RANS models. They assume that the Reynolds stress, mean strain, and two turbulence scale factors satisfy a linear or non-linear algebraic relationship. These turbulence scale factors can be derived from solving two transport equations of the model. The RNG k-ε model is suitable for side entry and inclined side entry jet stirring tank simulations, while the SST model is suitable for axial jet mixing tanks [30]. The SST model is a hybrid model combining the k-ω and k-ε models such that the k-ω model is used in the near-wall region and the k-ε model is carried out in the free shear flow [35-37]. The RSM model is another classical turbulence model. Unfortunately, it is not applied in the paper due to the high computational effort and poor convergence behavior. LES requires substantial computational power and is not possible for large-scale industrial devices at high Reynolds number [38]. Therefore, the RNG k-ε model and the SST model are used to predict oxygen-enriched air distribution in the stirring tank, and these turbulence models are compared based on the results obtained in **Section 2.5**. The SST model is chosen as the appropriate turbulence model for the simulation, which is algebraically described as follows [35]:

$$\frac{\mathrm{D}\rho k}{\mathrm{D}t} = \tau_{ij}\frac{\partial u_i}{\partial x_j} - \beta^* \rho\omega k + \frac{\partial}{\partial x_j}\left[\left(\mu + \sigma_k \mu_t\right)\frac{\partial k}{\partial x_j}\right], \tag{11}$$

7

$$\frac{\mathrm{D}\rho\omega}{\mathrm{D}t} = \frac{\gamma}{v_t}\tau_{ij}\frac{\partial u_i}{\partial x_j} - \beta\rho\omega^2 + \frac{\partial}{\partial x_j}\left[\left(\mu + \sigma_\omega\mu_t\right)\frac{\partial\omega}{\partial x_j}\right] + 2\left(1 - F_1\right)\rho\sigma_{\omega 2}\frac{1}{\omega}\frac{\partial k}{\partial x_j}\frac{\partial\omega}{\partial x_j}. \quad (12)$$

The blending function F_1 is defined as:

$$F_1 = \tanh\left(\mathrm{arg}_1^4\right), \quad (13)$$

$$\mathrm{arg}_1 = \min\left[\max\left(\frac{\sqrt{k}}{0.09\omega y}; \frac{500v}{y^2\omega}\right); \frac{4\rho\sigma_{\omega 2}k}{CD_{k\omega}y^2}\right], \quad (14)$$

where y represents the distance to the next surface and $CD_{k\omega}$ represents the positive part of the cross-diffusion term in Eq. (11).

The eddy viscosity is defined as:

$$v_t = \frac{a_1 k}{\max\left(a_1\omega; \Omega F_2\right)\omega}, \quad (15)$$

Where Ω represents the absolute value of the vorticity.

The blending function F_2 is defined as:

$$F_2 = \tanh\left(\mathrm{arg}_2^2\right), \quad (16)$$

$$\mathrm{arg}_2 = \max\left(2\frac{\sqrt{k}}{0.09\omega y}; \frac{500v}{y^2\omega}\right). \quad (17)$$

Moreover, the constants of SST turbulence model are: σ_{k1}=0.85, $\sigma_{\omega 1}$=0.5, β_1=0.0750, a_1=0.31, β^*=0.09.

The wall function y^+, the semi-empirical description of the near-wall region, is the complementary function of the turbulence model. In the near-wall region, ten layers are generated near walls with $y^+ \approx 1$ for the first layer.

2.3 Solver setup

The commercial CFD software ANSYS FLUENT 14.5 is used for the three-dimensional transient numerical simulation of the stirring tank. The value of

8

gravity is set at 9.8 m/s^2 and the gravity direction is along the -Z direction, as shown in Figure 1 (a). The finite volume method is carried out to discretize the incompressible Navier-Stokes equation. In order to ensure calculation accuracy, the continuous fluid is discretized by the delay-corrected QUICK difference, and for the diffusion phase, the upwind differential discretization is adopted. The coupling of pressure and velocity is solved using the SIMPLE algorithm. SIMPLE algorithm is widely used in the numerical calculation of N-S equations for both compressible and incompressible flows with all speeds [39]. The second-order upwind method is selected to solve momentum, kinetic energy, and turbulence dissipation rate equations.

To determine the influence of time step on the accuracy of numerical simulation results, the oxygen-enriched air distribution in cross-section $Z = 2$ and 10 m are compared when the time step is set at 0.05, 0.1, and 0.2 s, as shown in Figure 2. The area ratio occupied by oxygen-enriched air with the volume fraction ranging from 0.01 to 0.02 is close to 60% with the time step 0.05 and 0.10 s in the cross-section $Z = 2$ m and the overall distribution state is similar. While the time step is increased to 0.20 s, the oxygen-enriched air with a volume fraction below 0.01 appears at the edge of the stirring tank and occupies more than half the area. Moreover, the coverage area of high concentration air in the cross-section $Z = 10$ m is smaller than that under the conditions of 0.05 and 0.1 s, as shown in Figure 2 (b). It concludes that the time step 0.1 s is optimum for the simulation. To obtain a stable liquid flow field, simulate for 60 s without the oxygen-enriched air and then continue the computation introducing the oxygen-enriched air for 180 s. The total simulation time is 240 s.

2.4 Grid generation and boundary conditions

Considering that the dispersion of oxygen-enriched air is mainly concentrated in the lower part of the lime slurry stirring tank and the complex geometric structure, this region, particularly near rotary jet machines, is refined with tetrahedral meshes by GAMBIT. While hexahedron meshes are utilized for the upper part of the tank and air inlet pipes, as shown in Figure 3. Figure 4 presents the results of the grid-independence test in the distribution of oxygen-enriched air for three resolutions of mesh size in cross-sections $Z = 2$ and 10 m. For the negligible difference in the numerical results between 1.85 million and 2.17 million grids, the model with 1.85 million grids is employed for further study with the consideration of computational efficiency and grid sensitivity.

The flow in the stirring tank contains liquid and gas phases. The Eulerian model is adopted to represent the multiphase flow behavior. The rotation jet machines rotate at an angular velocity ω ranging from 0.1 to 1 rad/s in practice and the liquid-phase ejects from the nozzle at an outlet velocity v. The outlet velocity can be adjusted in the range of 35 to 65 m/s, as shown in Table 2. The liquid phase is the standard liquid water, and the liquid phase inlet is defined as the velocity inlet. The outlet is defined as the pressure outlet. The standard air is chosen as the gas phase and is injected from the inlet pipe with the mass flow rate fixed to 1.2 kg/s. Therefore, the gas phase inlet is defined as the mass flow inlet. The connection between the upper and lower part of the stirring tank is set to interface and the remaining walls are defined as no-slip boundary conditions.

10

2.5 Validation of the numerical model

To confirm the correctness of the numerical model, it is necessary to validate the consistency of the results of the numerical simulation and available experiment data under the identical condition. The experimental data of the liquid flow rate of an IM20 rotary jet machine is obtained from the previous work of Nordkvist et al. [40]. Figure 5 presents the comparison of the experimental data and the corresponding simulated liquid flow rate results.

The experimental volumetric liquid flow rate (ordinate) of the rotary jet nozzle is obtained at aerated conditions. The outlet diameter of the nozzle is constant (10 mm). The difference in nozzle inlet pressure leads to a change in the velocity of the liquid and the liquid flow rate varies consequently. The closer the simulated results are to the diagonal line in Figure 5, the more consistent they are with the experimental results. Excellent agreement between the numerical results using the SST turbulence model and the referenced experimental data indicates that the numerical method used in this study is able to accurately capture the physical characters in the rotary jet machine stirring system.

3. Results and discussion

In order to intuitively analyze the influence of angular rotation velocity and outlet velocity on the axial distributions of oxygen-enriched air, draw monitoring lines L-1 and L-2 through the points (5400, -3100, 0) near air inlet pipe No.1 and (4000, 4700, 0) near air inlet pipe No.2, respectively. L-1 and L-2 are parallel to the Z-axis. Likewise, draw the monitoring line L-3 through the origin of coordinates, which

11

coincides with the Z-axis, as shown in Figure 1 (b). The monitoring lines are chosen according to the oxygen-enriched air concentration. That is, the concentration is the highest near the inlet pipe, while it reduces to a minimum at the region farthest from the pipe.

3.1 Influence of angular rotation velocity on oxygen-enriched air concentration

The uniform distribution of oxygen-enriched air, which is the prerequisite for the effectiveness of all forced oxidation processes, means that the concentration of oxygen-enriched air is maintained at a stable value after emerging from the inlet pipe, and its concentration gradient is as small as possible. Moreover, a high concentration of oxygen-enriched air facilitates the forced oxidation process. Figure 6 shows the oxygen-enriched air volume fraction on lines L-1 (Figure 6 (a)), L-2 (Figure 6 (b)), and L-3 (Figure 6 (c)) at various angular velocities. For L-1, the range of the peak value of volume fraction is from the height of 2.5 to 5 m at 0.50 and 1.00 rad/s. When the height is greater than 5 m, the volume fraction of oxygen-enriched air rapidly decreases to 0.02–0.03, which indicates that it is difficult for the rotary jet machine to prevent the formation of the volume fraction peak region near the air inlet pipes. In the cases of 0.10 and 0.25 rad/s, the peak values appear on 1 and 4.5 m above the inlet pipe, respectively. But their values are much lower than those of the other two conditions. The double peak curves of the volume fraction of oxygen-enriched air appear on L-2, as shown in Figure 6 (b). Compared with L-1, the amount of the peak values at 0.10 and 0.25 rad/s are largely increased, while there is a declining trend for the peak values at 0.50 and 1.00 rad/s. Therefore, the concentration of

12

oxygen-enriched air in L-2 is less uniform than that in L-1 at 240 s.

The distance between the monitoring line L-3 and the oxygen-enriched air inlet pipe is the farthest. Therefore, there is a disadvantage in the center of the stirring tank for the accumulation of oxygen-enriched air., as shown in Figure 6 (c). The peak value appears in the range of 0–4 m from the bottom of the tank and the maximum peak value is 0.02 at 0.10 rad/s. Figure 7 shows the volume fraction contour of oxidation on the cross-section Z = 10 m at various angular velocities. The volume fraction is reduced to 0 at 0.50 rad/s above the cross-section Z = 9 m, which can be verified by Figure 7 (c). The distributions of oxygen-enriched air fluctuate greatly in L-3 because the air swims upward in the center of the tank after it is impacted by the downward flowing liquid.

For the upper part of the stirring tank, the distribution of oxygen-enriched air tends to be homogeneous and then deteriorate with the increase in rotation angular velocity. The oxygen-enriched air can cover most regions of the cross-section and the concentration gradient is small at a rotation angular velocity of 0.25 rad/s, as shown in Figure 7 (b). Figure 8 (a) also reflects this distribution pattern. Under this working condition where the volume fraction of oxygen-enriched air is less than 0.02, the area ratio is significantly smaller than that under the conditions with rotation angular velocities of 0.10, 0.50, and 1.00 rad/s. The proportion of area with the volume fraction of 0.02–0.1 exceeds 60% at the angular velocity of 0.25 rad/s. Whereas, for all other conditions, this percentage does not exceed 40%. The accumulation of oxygen-enriched air seriously affects the effect of forced oxidation. Therefore, for the

stirring tank with an angular velocity of 0.25 rad/s, the concentration of oxygen-enriched air is already sufficient for the necessary reaction of calcium sulfite with oxygen in the region of the cross-section $Z = 10$ m. In addition, the volume fraction of oxygen-enriched air in 90 % of the area is in the range of 0.01 to 0.05, which means that the air is evenly distributed.

There are slanted nozzles with an angle of 30° between the central axis and the horizontal plane on the jet agitator, and the jet ejects obliquely from these nozzles. The presence of slanted nozzles makes the flow field more intense in the lower part of the stirring tank (Figure 8 (b) and Figure 9). With the increase in the rotation angular velocity, the volume fraction of oxygen-enriched air firstly becomes more homogeneous, however, later its fractions deteriorate. The oxygen-enriched air can be evenly distributed on the cross-section $Z = 2$ m at 0.10 and 0.25 rad/s, as shown in Figure 9 (a) and (b). The volume fraction in the range from 0.01 to 0.025 occupies more than 80% of the cross-sectional area. In addition, there is no large gradient change of the volume fraction. Even at the weak link of oxygen-enriched air distribution L-3 (Figure 6 (c)), the volume fraction at low rotation angular velocities is greater than that at high rotation angular velocities. Large-scale areas with near-zero concentration at rotation angular velocities of 0.50 and 1.00 rad/s, as shown in Figure 9 (c) and (d), and the oxygen-enriched air accumulates locally. At a rotation angular velocity of 0.5 rad/s, the area with a volume fraction of less than 0.01 accounts for approximately 40%, which is quadruple that at 0.10 rad/s. It can be concluded that the low rotation angular velocity facilitates the homogenization of oxygen-enriched air

for the lower part of the tank.

In summary, with the increase in the rotation angular velocity, the distribution of oxygen-enriched air is increasingly homogeneous at first, but later deteriorates. The oxygen-enriched air distribution with a rotation angular velocity of 0.25 rad/s is superior to other conditions in terms of concentration fluctuation range and gradient.

3.2 Influence of jet outlet velocity on oxygen-enriched air concentration

The jet outlet velocity is also a critical factor affecting the concentration of oxygen-enriched air. Its chaotic extent can be significantly improved with the increase in the jet outlet velocity in the stirring tank. According to Figure 10 (a), peak curves are similar under all conditions on cross-section $Z = 4$ m on L-1, and peak values increase and then decrease with the increase of jet outlet velocity. The peak value reaches the maximum up to 0.3 at 45 m/s. As the height increases, the volume fraction of oxygen-enriched air maintains a relatively stable value at outlet velocities of 35, 55, and 65 m/s. However, the volume fraction fluctuates greatly at 45 m/s and is reduced to 0 above the cross-section $Z = 13$ m. Figure 10 (b) shows that the peak value also appears 4 m above the bottom of the tank on L-2. Peak values slightly increase at 35 and 45 m/s compared with that on L-1. While peak values are declined significantly with the outlet velocities of 55 and 65 m/s, indicating that the discrete effect of turbulence near the inlet pipe No.2 is more conspicuous than that near inlet pipe No.1. Peak values formed in the range of 0–4 m above the bottom of the tank show a trend of increasing first and then decreasing with the increase of jet outlet velocity, as shown in Figure 10 (c). Fortunately, near-zero concentration areas, where the volume

fraction of oxygen-enriched air is lower than 0.005, only exist near the bottom of the stirring tank in L-3.

Under low part jet outlet velocities within the upper part of the stirring tank, the distribution of oxygen-enriched air is extremely (Figure 11 (a) and (b)). The intensity of the turbulent layer is not large enough under working conditions No.5 and 6, resulting in inefficient stirring performance. The oxygen-enriched air is concentrated and there are extensive low-concentration regions on the cross-section $Z = 10$ m. Figure 12 shows the area ratio of different volume fractions of oxygen-enriched air on cross-sections $Z = 10$ and 2 m at different jet outlet velocities. When jet outlet velocities reach 45 m/s, even the region with the volume fraction of 0–0.01 covers 61.33% of the cross-sectional area (Figure 12 (a)), while the distribution of oxygen-enriched air is improved as the jet outlet velocity increases, as shown in Figure 11 (c) and (d). Under these conditions, the distribution range of highly concentrated oxygen-enriched air is vast, and the concentration gradient is small. The difference between the central area and the tank wall is minor, and the overall concentration is in the range of 0.01–0.05. Comparing Figure 11 (c) with (d), the volume fraction of oxygen-enriched air in the center of the tank does not increase correspondingly as the jet outlet velocity increases from 55 to 65 m/s (see Figure 10 (c)).

For the lower part of the stirring tank, the distribution of oxygen-enriched air tends to be firstly homogeneous and then non-uniform (Figure 12 (b) and 13). Large-scale near-zero concentration regions appear in Figure 13 (a) and (d), and

approximately 90% of the area in the cross-section has the volume fraction of 0–0.015. While the oxygen-enriched air can be distributed evenly on the cross-section $Z = 2$ m at 45 and 55 m/s, and the volume fraction ranges from 0.005 to 0.025 in the area with an area ratio of approximately 90%. Among them, the region with the volume fraction of 0.015–0.025 covers more than 60% of the cross-sectional area in Figure 13 (b), indicating that oxygen-enriched air is maintained at high concentrations in most areas. Unfortunately, the distribution of oxygen-enriched air on the cross-section $Z = 10$ m under the same condition is mostly uneven, which illustrates that the air concentration fluctuates greatly within the entire stirring tank and is adverse to the forced oxidation of calcium sulfate.

In summary, with different jet outlet velocities, we can observe a considerable discrepancy in the distribution of oxygen-enriched air. The quality of oxygen-enriched air distribution is also different at different heights of the stirring tank. At a jet outlet velocity of 55 m/s the distribution of oxygen-enriched air reaches the highest conductivity and is most conducive to the process of forced oxidation.

4. Conclusion

In order to improve the oxidation of calcium sulfate, rotary jet machines were used to homogenize oxygen-enriched air in a full-scale lime slurry desulfurization system. The effects of rotation angular velocity and jet outlet velocity on the distribution of oxygen-enriched air were numerically investigated and the next conclusions were drawn:

(1) Both rotation angular velocity and jet outlet velocity significantly affected the

17

distribution of oxygen-enriched air. The distribution of oxygen-enriched air was optimal when the rotation angular ω and the jet outlet velocities v reached 0.25 rad/s and 55 m/s, respectively.

(2) The chaotic forces within the lime slurry tank were promoted with the increase in rotation angular and jet outlet velocities. However, the chaotic degree is not linearly related to the homogenization of oxygen-enriched air, and it is not that the greater the chaotic degree is, the more homogeneous the oxygen-enriched air is.

(3) Under the optimal condition ($\omega = 0.25$ rad/s, $v = 55$ m/s), the volume fraction of the oxygen-enriched air was greater than zero in the whole stirring tank, and the distribution of oxygen-enriched air was uniform. The rotary jet stirring system could obtain a satisfactory stirring effect, which avoided the segregated phenomenon existing in mechanical agitators.

In the future, further research on the oxidation reaction process of hydrated calcium sulfite in the stirring tank and the stability analysis and optimization of rotary jet agitators are needed.

Acknowledgement

Reference

[1] J. Heo, P.J. Adams, H.O. Gao, Public Health Costs of Primary PM2.5 and Inorganic PM2.5 Precursor Emissions in the United States, Environ Sci Technol 50 (2016) 6061-6070.

[2] D. Vallero, Chapter 16 - Scale and Complexity of Air Pollution, in: D. Vallero (Ed.) Fundamentals of Air Pollution (Fifth Edition), Academic Press, Boston, 2014, pp. 381-412.

[3] Z. Li, C. Xie, J. Lv, R. Zhai, Effect of calcium formate as an additive on desulfurization in power plants, J Environ Sci (China) 67 (2018) 89-95.

[4] D. Graves, J.J. Smith, L. Chen, A. Kreinberg, B. Wallace, R. White, Biogeochemical oxidation of calcium sulfite hemihydrate to gypsum in flue gas desulfurization byproduct using

sulfur-oxidizing bacteria, J Environ Manage 201 (2017) 357-365.

[5] H. Bin, Y. Yang, Y. Chunmin, Z. Lin, Y. Linjun, Improving the electrostatic precipitation removal efficiency by desulfurized wastewater evaporation, RSC Advances 6 (2016) 113703-113711.

[6] R. del Valle-Zermeño, J. Formosa, J.M. Chimenos, Wet flue gas desulfurization using alkaline agents, Reviews in Chemical Engineering 31 (2015).

[7] B.B. Hansen, S. Kiil, Investigation of Parameters Affecting Gypsum Dewatering Properties in a Wet Flue Gas Desulphurization Pilot Plant, Industrial & Engineering Chemistry Research 51 (2012) 10100-10107.

[8] G.C. Potter, F.A. Kummerow, A SIMPLE JET TYPE AIR STIRRER, Science 110 (1949) 592-592.

[9] P. Han, X.-j. Mao, L.-h. Zhou, S.-m. Jiao, Mechanism modeling for forced oxidation system of flue gas desulfurization device, J. North China Electr. Power Univ. (China) 33 (2006) 60-63.

[10] V. Roussinova, S.M. Kresta, R. Weetman, Low frequency macroinstabilities in a stirred tank: Scale-up and prediction based on large eddy simulations, Chemical Engineering Science 58 (2003) 2297-2311.

[11] M.X. Zhang, Y.Y. Hu, W.T. Wang, T. Shao, Y. Cheng, Intensification of viscous fluid mixing in eccentric stirred tank systems, Chem. Eng. Process. 66 (2013) 36-43.

[12] M. Eng, A. Rasmuson, Large Eddy Simulation of the influence of solids on macro instability frequency in a stirred tank, Chemical Engineering Journal 259 (2015) 900-910.

[13] J. Kosel, I. Gutiérrez-Aguirre, N. Rački, T. Dreo, M. Ravnikar, M. Dular, Efficient inactivation of MS-2 virus in water by hydrodynamic cavitation, Water Research 124 (2017) 465-471.

[14] A. Sarc, J. Kosel, D. Stopar, M. Oder, M. Dular, Removal of bacteria Legionella pneumophila, Escherichia coli, and Bacillus subtilis by (super)cavitation, Ultrason Sonochem 42 (2018) 228-236.

[15] J. Kosel, A. Sinkovec, M. Dular, A novel rotation generator of hydrodynamic cavitation for the fibrillation of long conifer fibers in paper production, Ultrason Sonochem 59 (2019) 104721.

[16] M. Sežun, J. Kosel, M. Zupanc, M. Hočevar, J. Vrtovšek, M. Petkovšek, M. Dular, Cavitation as a Potential Technology for Wastewater Management – An Example of Enhanced Nutrient Release from Secondary Pulp and Paper Mill Sludge, Strojniški vestnik – Journal of Mechanical Engineering 65 (2019) 641-649.

[17] J. Kosel, M. Sustarsic, M. Petkovsek, M. Zupanc, M. Sezun, M. Dular, Application of (super)cavitation for the recycling of process waters in paper producing industry, Ultrason Sonochem 64 (2020) 105002.

[18] X. Sun, J. Liu, L. Ji, G. Wang, S. Zhao, J.Y. Yoon, S. Chen, A review on hydrodynamic cavitation disinfection: The current state of knowledge, Sci Total Environ 737 (2020) 139606.

[19] A.R. Ismagilov, E.K. Spiridonov, O.V. Belkina, Liquid Jet Ejector Efficiency Improvement, in: A.A. Radionov (Ed.) International Conference on Industrial Engineering2017, pp. 99-106.

[20] W. Bartok, C.E. Heath, M.A. Weiss, Mixing in a Jet-Stirred Reactor, Aiche Journal 6 (1960) 685-687.

[21] T.Y. Amiri, J. Moghaddas, Experimental Study of the Mixing Time in a Jet-Mixed Gas-Liquid System, Chemical Engineering & Technology 33 (2010) 327-333.

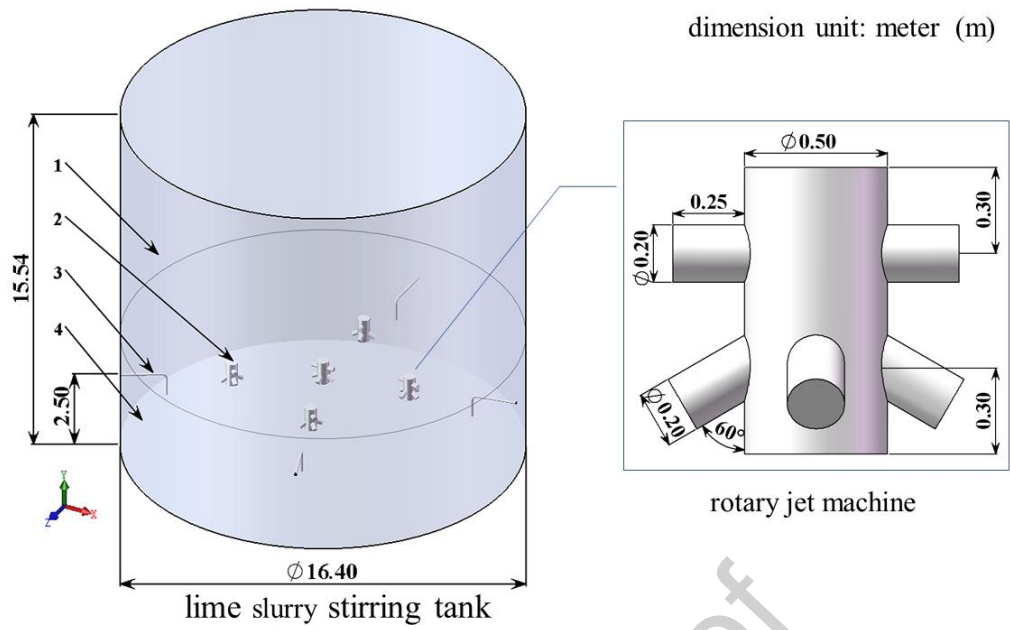[22] T.Y. Amiri, J.S. Moghaddas, Y. Moghaddas, A jet mixing study in two phase gas–liquid

systems, Chemical Engineering Research and Design 89 (2011) 352-366.

[23] J. Claesson, A. Rasmuson, J. Wiklund, T. Wikstrom, Measurement and Analysis of Flow of Concentrated Fiber Suspensions through a 2-D Sudden Expansion Using UVP, Aiche Journal 59 (2013) 1012-1021.

[24] L.F. Zhang, F. Li, Investigation on the Fluid Flow and Mixing Phenomena in a Ruhrstahl-Heraeus (RH) Steel Degasser Using Physical Modeling, Jom 66 (2014) 1227-1240.

[25] M. Qin, Y. Dong, L. Cui, J. Yao, C. Ma, Pilot-scale experiment and simulation optimization of dual-loop wet flue gas desulfurization spray scrubbers, Chemical Engineering Research and Design 148 (2019) 280-290.

[26] K.V. Sharp, R.J. Adrian, PIV study of small-scale flow structure around a Rushton turbine, Aiche Journal 47 (2001) 766-778.

[27] M. Rahimi, A. Parvareh, Experimental and CFD investigation on mixing by a jet in a semi-industrial stirred tank, Chemical Engineering Journal 115 (2005) 85-92.

[28] L. Furman, Z. Stegowski, CFD models of jet mixing and their validation by tracer experiments, Chem. Eng. Process. 50 (2011) 300-304.

[29] J.M. Mejia, A. Sadiki, A. Molina, F. Chejne, P. Pantangi, Large Eddy Simulation of the Mixing of a Passive Scalar in a High-Schmidt Turbulent Jet, Journal of Fluids Engineering-Transactions of the Asme 137 (2015).

[30] B. Sajjadi, A.A.A. Raman, S. Ibrahim, R.S.S.R.E. Shah, Review on gas-liquid mixing analysis in multiscale stirred vessel using CFD, Reviews in Chemical Engineering 28 (2012).

[31] R.K. Wang, H.X. Wang, S.Y. Chen, Y.P. Qu, C. Wang, Numerical investigation of multiphase flow in flue gas desulphurization system with rotary jet stirring, Results Phys 7 (2017) 1274-1282.

[32] Y. Qu, C. Zhou, Y. Zhong, S. Chen, R. Wang, A computational study on gas–liquid flow in a lime slurry pond equipped with a rotary jet mixing system, Advances in Mechanical Engineering 9 (2017).

[33] E. Bumrungthaichaichan, A review on numerical consideration for computational fluid dynamics modeling of jet mixing tanks, Korean Journal of Chemical Engineering 33 (2016) 3050-3068.

[34] X. Sun, S. Kim, S.D. Yang, H.S. Kim, J.Y. Yoon, Multi-objective optimization of a Stairmand cyclone separator using response surface methodology and computational fluid dynamics, Powder Technology 320 (2017) 51-65.

[35] F.R. Menter, Two-equation eddy-viscosity turbulence models for engineering applications, AIAA Journal 32 (1994) 1598-1605.

[36] X. Sun, X. Xuan, Y. Song, X. Jia, L. Ji, S. Zhao, J. Yong Yoon, S. Chen, J. Liu, G. Wang, Experimental and numerical studies on the cavitation in an advanced rotational hydrodynamic cavitation reactor for water treatment, Ultrason Sonochem 70 (2021) 105311.

[37] X. Sun, W. You, X. Xuan, L. Ji, X. Xu, G. Wang, S. Zhao, G. Boczkaj, J.Y. Yoon, S. Chen, Effect of the cavitation generation unit structure on the performance of an advanced hydrodynamic cavitation reactor for process intensifications, Chemical Engineering Journal 412 (2021).

[38] J.B. Joshi, N.K. Nere, C.V. Rane, B.N. Murthy, C.S. Mathpati, A.W. Patwardhan, V.V. Ranade, CFD simulation of stirred tanks: Comparison of turbulence models. Part I: Radial flow impellers, The Canadian Journal of Chemical Engineering 89 (2011) 23-82.

[39] J.H. Ferziger, Computational methods for fluid dynamics, 3rd ed., springer, Berlin, 2012.

[40] M. Nordkvist, T. Grotkjaer, J.S. Hummer, J. Villadsen, Applying rotary jet heads for mixing

and mass transfer in a forced recirculation tank reactor system, Chemical Engineering Science 58 (2003) 3877-3890.

Figures

dimension unit: meter (m)

1-upper part   2-rotation jet system   3-oxidation air inlet pipe   4-lower part
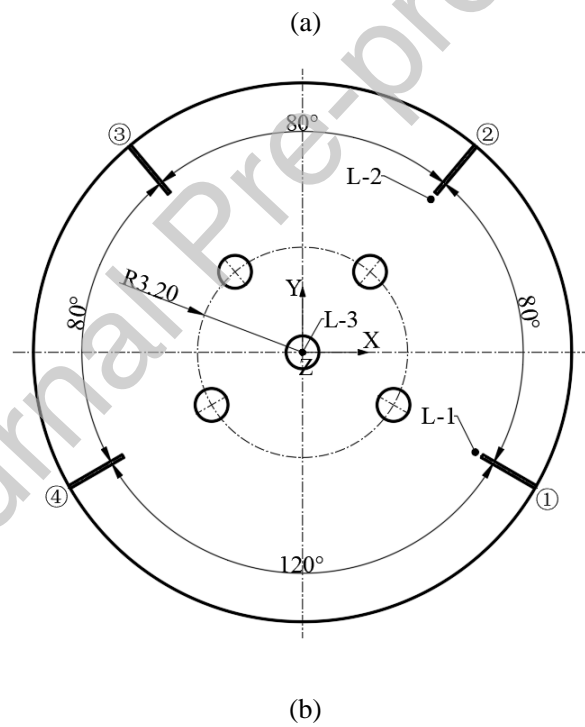
(a)

(b)

Figure 1 Physical model of lime slurry tank: (a) overall structure of the tank, (b) distribution of rotary jet machines.
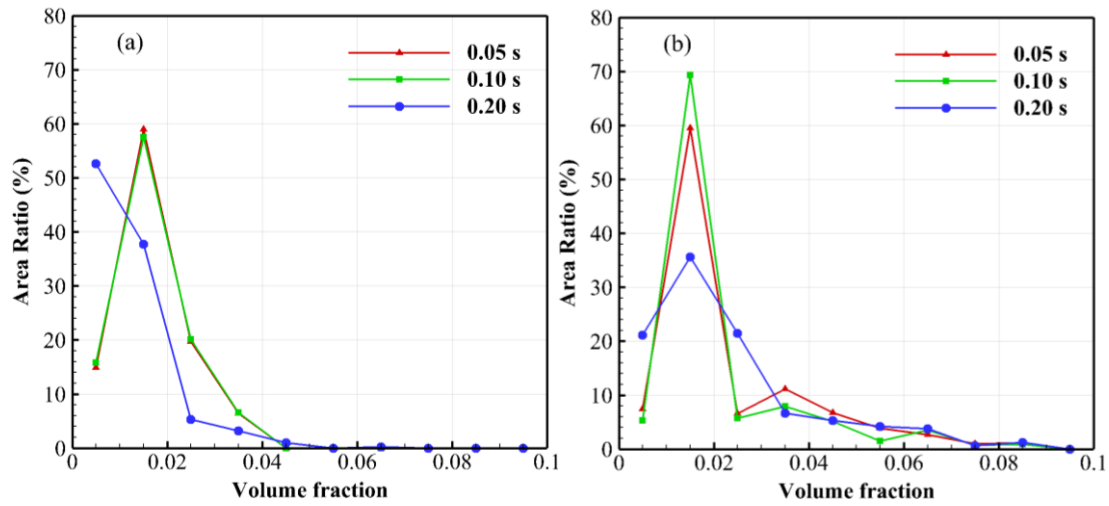
24

Figure 2 Area ratio for different concentrations of oxidation air in the cross-sections

(a) Z = 2 m and (b) Z = 10 m with different time steps.
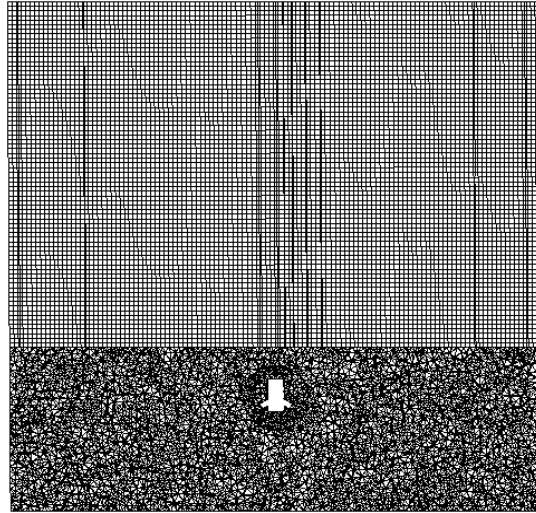
Figure 3 Mesh generation of the stirring tank model.
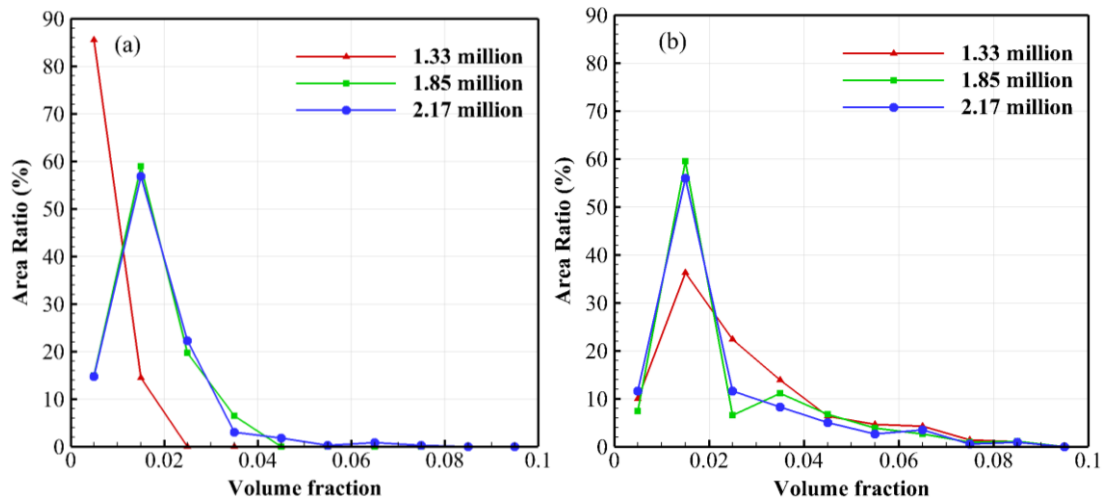
Figure 4 Area ratio for different concentrations of oxidation air in the cross-sections

(a) Z = 2 m and (b) Z = 10 m with different number of grids.
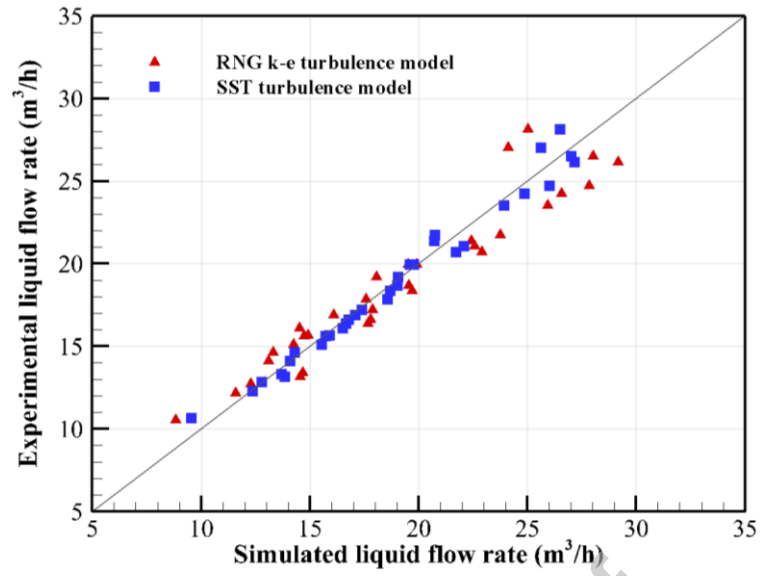
Figure 5 Comparison between the experimental data and simulation results for liquid

flow rate [33].

28
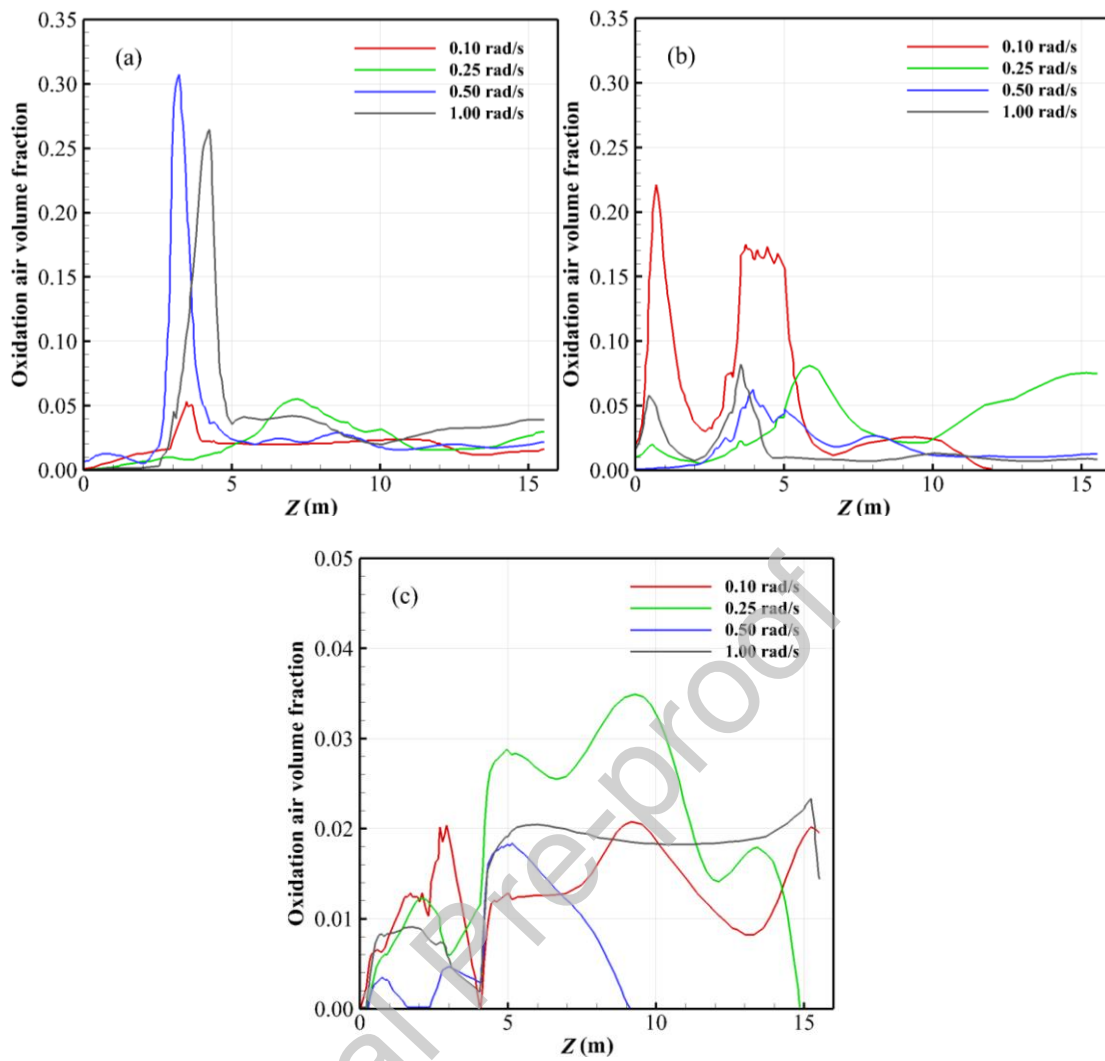
Figure 6 Oxidation air volume fraction curves on lines (a) L-1, (b) L-2, and (c) L-3

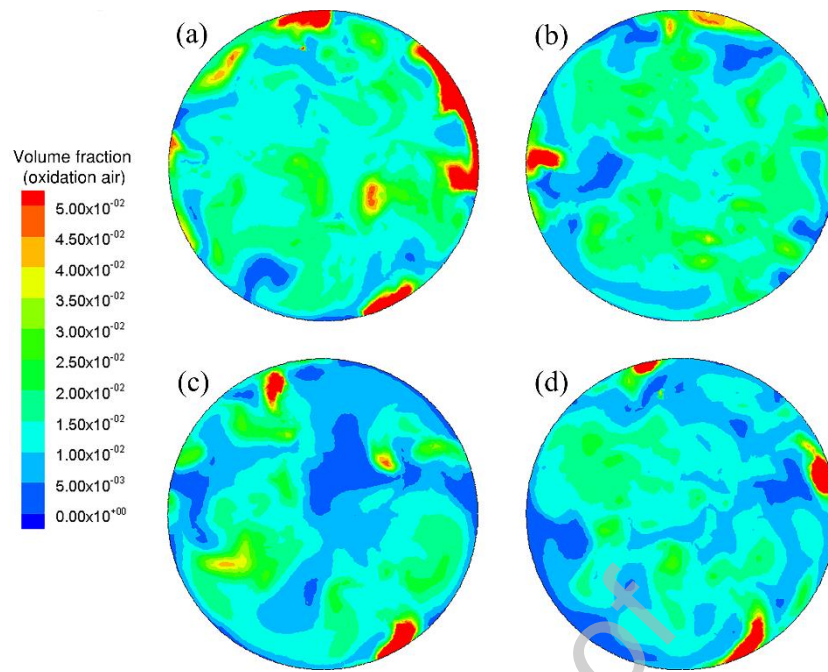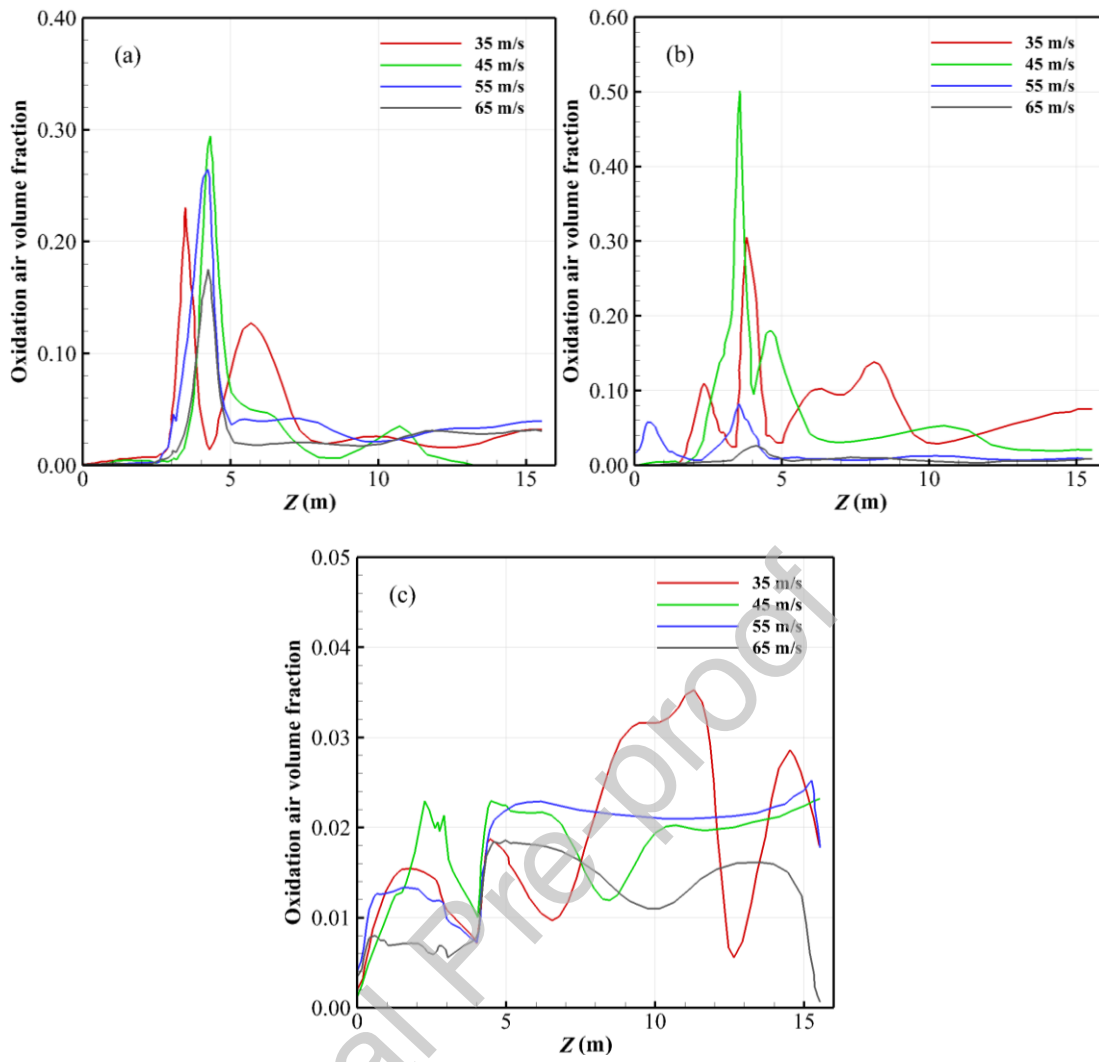under conditions with different angular velocities.

29
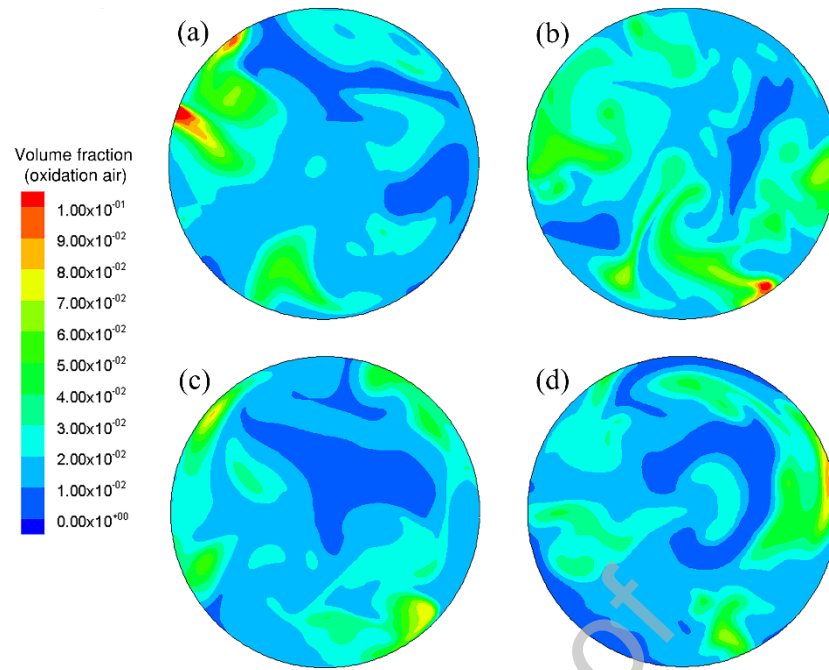
Figure 7 Volume fraction contour of oxidation air in the cross-section Z = 10 m at
angular velocities of (a) 0.10, (b) 0.25, (c) 0.50, and (d) 1.00 rad/s.
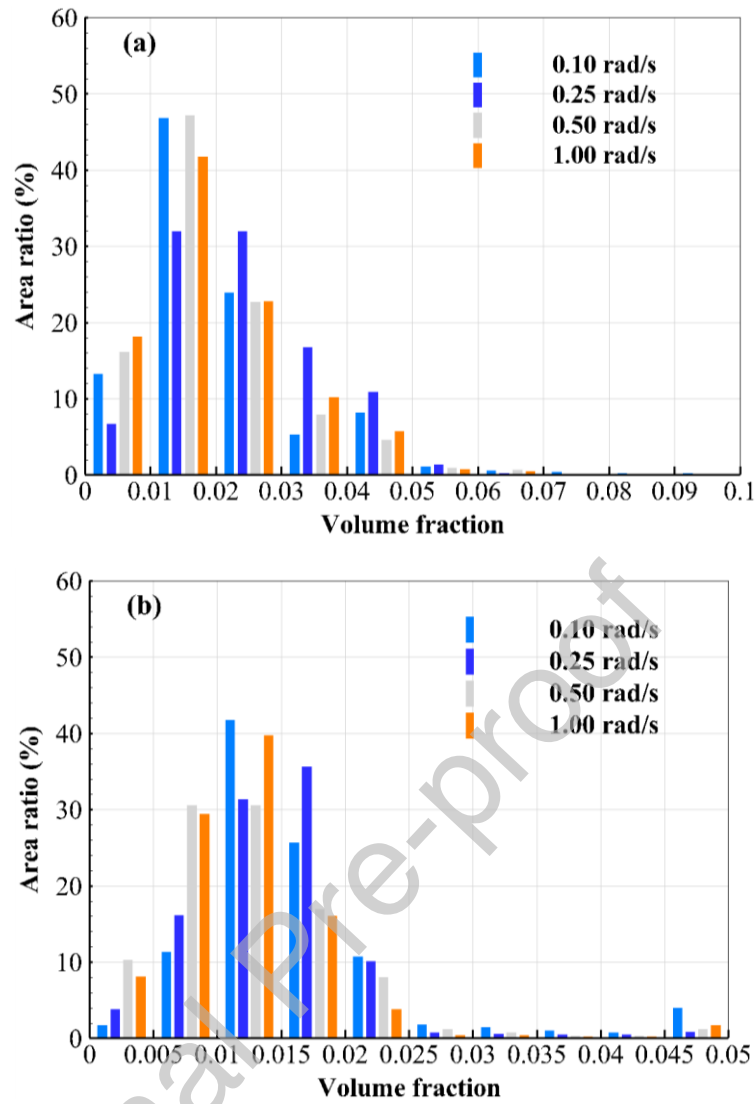
Figure 8 Area ratio of different volume fraction of oxidation air on cross-sections (a) Z = 10 m and (b) Z = 2 m at different angular velocities.

31

Figure 9 Volume fraction contour of oxidation air on cross-section Z = 2 m at angular velocities of (a) 0.10, (b) 0.25, (c) 0.50, and (d) 1.00 rad/s.

Figure 10 Oxidation air volume fraction curves on lines (a) L-1, (b) L-2, and (c) L-3

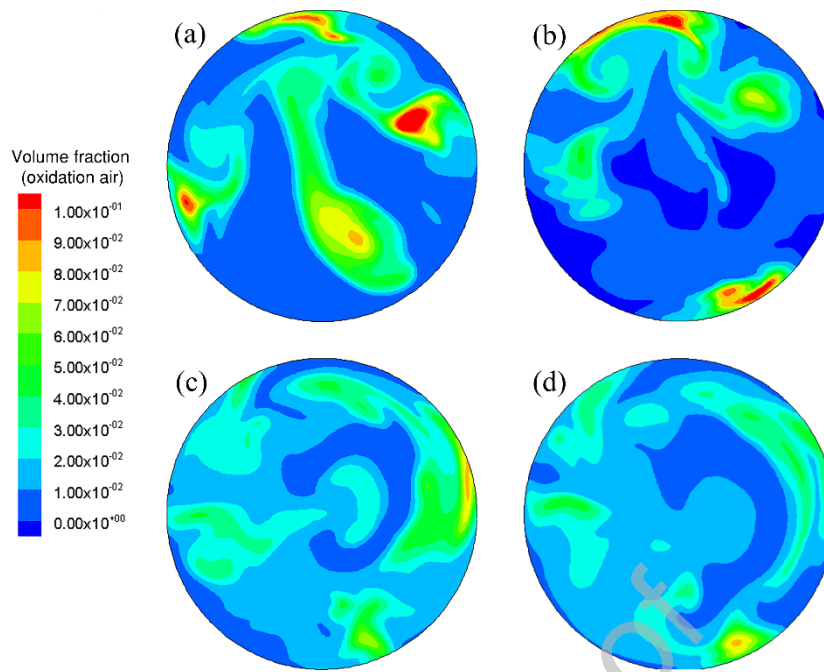under conditions with different jet outlet velocities.

33

Figure 11 Volume fraction contour of oxidation air on the cross-section Z = 10 m at jet outlet velocities of (a) 35, (b) 45, (c) 55, (d) 65 m/s.
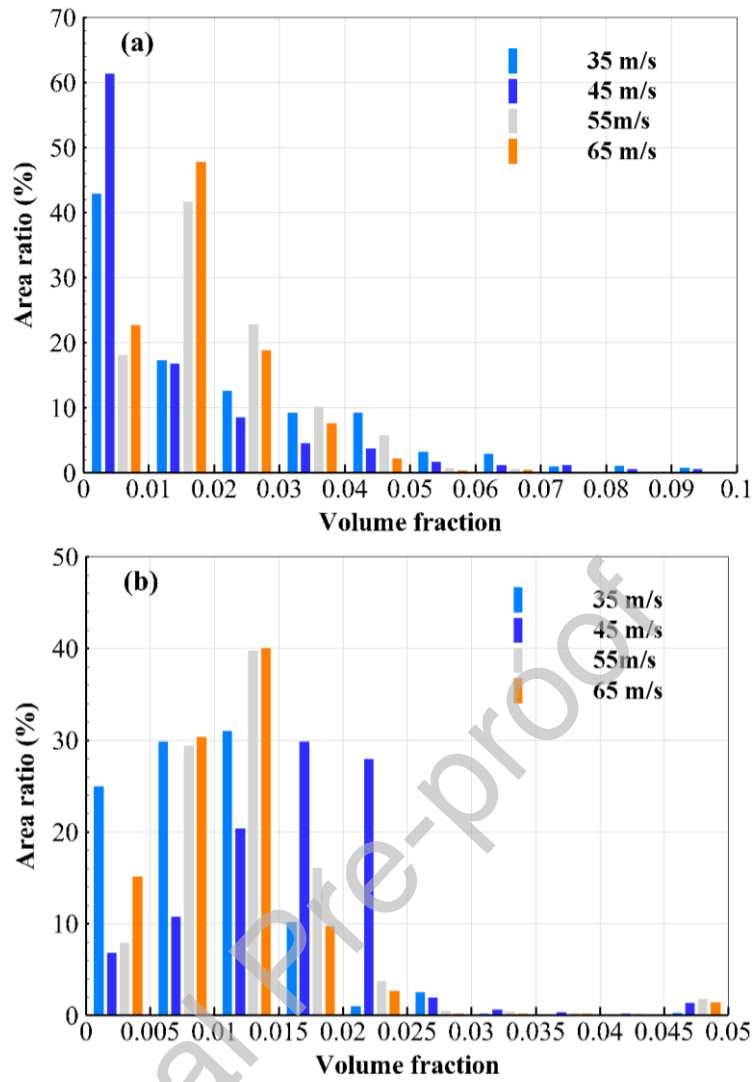
Figure 12 Area ratio of different volume fraction of oxidation air on the cross-sections (a) Z = 10 m and (b) Z = 2 m at different jet outlet velocities.
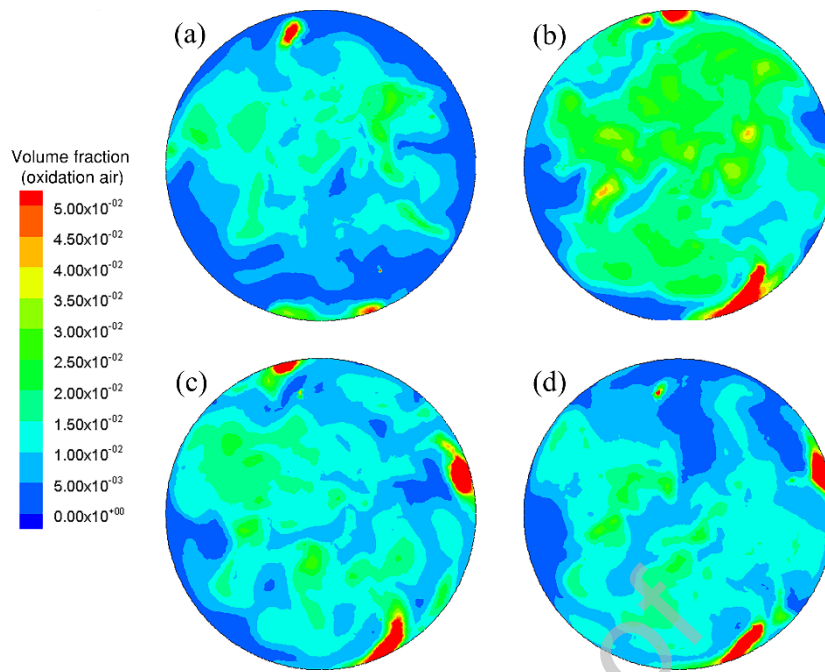
Figure 13 Volume fraction nephograms of oxidation air on the cross-section $Z = 2$ m with jet outlet velocities of (a) 35, (b) 45, (c) 55, and (d) 65 m/s.

Tables

Table 1 Rate determining steps and reactions in WFGD technology [19].

Rate determining step	Reaction	
Absorption of SO_2 in water	$SO_2 + H_2O \rightleftharpoons H^+ + HSO_3^-$	(1)
	$HSO_3^- \rightleftharpoons H^+ + SO_3^{2-}$	(2)
Oxidation of HSO_3^-	$HSO_3^- + \frac{1}{2}O_2 \rightleftharpoons H^+ + SO_4^{2-}$	(3)
	$HSO_4^- \rightleftharpoons SO_4^{2-} + H^+$	(4)
Limestone dissolution	$CaCO_3 \rightleftharpoons Ca^{2+} + CO_3^{2-}$	(5)
	$CO_2 + H_2O \rightleftharpoons HCO_3^- + H^+$	(6)
	$HCO_3^- \rightleftharpoons CO_3^{2-} + H^+$	(7)
	$H_2O \rightleftharpoons H^+ + OH^-$	(8)
Gypsum crystallization	$Ca^{2+} + SO_4^{2-} + 2H_2O \rightleftharpoons CaSO_4 \cdot 2H_2O$	(9)

1

Table 2 Condition parameters of WFDG system.

Case	Working Condition	
	v (m/s)	ω (rad/s)
1	55	0.1
2	55	0.25
3	55	0.5
4	55	1
5	35	1
6	45	1
7	65	1

Author Statement

Longhao Xiang: Investigation, Methodology, Writing - Original Draft. Xun Sun: Writing - Review & Editing. Xuesong Wei: Writing - Review & Editing, Data Curation. Guichao Wang: Writing - Review & Editing. Grzegorz Boczkaj: Writing - Review & Editing. Joon Yong Yoon: Conceptualization, Supervision. Songying Chen: Writing - Review & Editing.

Declaration of interests

The authors declare that they have no known competing financial interests or personal relationships that could have appeared to influence the work reported in this paper.